Article:

Yao, M., Tang, H. orcid.org/0000-0002-2924-0126 and Huang, G. (2025) Roles of external forcing and internal variability in winter precipitation changes over central Asia. Earth's Future, 13 (7). e2025EF006064. ISSN 2328-4277

https://doi.org/10.1029/2025EF006064

AGU ADVANCING EARTH AND SPACE SCIENCES

Earth's Future

RESEARCH ARTICLE
10.1029/2025EF006064

Key Points:
- Greenhouse gas forcing favors increases in winter precipitation in Central Asia over multi-decadal timescales
- Phase transitions of Atlantic Multidecadal Variability play a dominant role in shaping winter precipitation trends in Central Asia
- Limiting global warming delays the emergence of increased winter precipitation in Central Asia beyond natural climate variability

Supporting Information:
Supporting Information may be found in the online version of this article.

Correspondence to:
H. Tang and G. Huang,
haosu.tang@sheffield.ac.uk;
hg@mail.iap.ac.cn

Citation:
Yao, M., Tang, H., & Huang, G. (2025). Roles of external forcing and internal variability in winter precipitation changes over Central Asia. *Earth's Future*, *13*, e2025EF006064. https://doi.org/10.1029/2025EF006064

Received 11 FEB 2025
Accepted 27 JUN 2025

Author Contributions:
Conceptualization: Haosu Tang
Data curation: Mengyuan Yao
Formal analysis: Mengyuan Yao, Haosu Tang
Funding acquisition: Gang Huang
Investigation: Mengyuan Yao
Methodology: Mengyuan Yao, Haosu Tang
Project administration: Gang Huang
Resources: Mengyuan Yao
Software: Mengyuan Yao
Supervision: Haosu Tang, Gang Huang
Validation: Mengyuan Yao
Visualization: Mengyuan Yao
Writing – original draft: Mengyuan Yao

Roles of External Forcing and Internal Variability in Winter Precipitation Changes Over Central Asia

Mengyuan Yao[1,2], Haosu Tang[3], and Gang Huang[1,2]

[1]State Key Laboratory of Earth System Numerical Modeling and Application, Institute of Atmospheric Physics, Chinese Academy of Sciences, Beijing, China, [2]University of Chinese Academy of Sciences, Beijing, China, [3]School of Geography and Planning, University of Sheffield, Sheffield, UK

Abstract Winter Central Asian precipitation (WCAP) is increasingly replacing snowfall as a critical water resource under global warming. Observations show a decline in WCAP from 1891 to 1946, followed by a recovery from 1947 to the recent decade. However, the relative contributions of external forcing and internal variability to these changes remain unclear. By analyzing observations and climate model simulations, this study finds that greenhouse gas forcing favors increasing WCAP, potentially offsetting drying trends driven by anthropogenic aerosols. Internal variability, primarily the phase transition of Atlantic Multidecadal Variability (AMV), plays a dominant role in shaping WCAP trends. The AMV-induced Rossby wave train, sustained by extracting baroclinic energy from the background mean flow, triggers barotropic atmospheric circulation anomalies that modulate WCAP. The cold-to-warm AMV phase transition (1891–1946) weakened the externally forced upward precipitation trend, reducing it from 0.19 to −0.20 mm month^{-1} decade^{-1}. In contrast, the warm-to-cold phase transition (1947–1997) amplified the externally forced precipitation trend, increasing it from 0.28 to 0.99 mm month^{-1} decade^{-1}. Under the high-emission future scenario, the time of emergence of externally driven WCAP increases is projected to occur between 2030 and 2060, at least a decade earlier than the post-2060 timeline projected under the medium-emission scenario. These findings underscore the critical role of AMV in shaping WCAP variability and highlight the necessity of emission reductions to delay the time when externally driven precipitation increases exceed the region's adaptive capacity.

Plain Language Summary Winter snowfall and spring meltwater are crucial water resources for water-scarce Central Asia (CA). However, with global warming, snowfall is increasingly shifting to occur as winter Central Asian precipitation (WCAP), influencing the region's hydrological cycle. Observations reveal a decline in WCAP from 1891 to 1946, followed by a recovery afterward. This study examines the roles of external forcing and internal variability in driving these trends. The findings indicate that external forcing weakly increases WCAP over the entire period. Greenhouse gas forcing significantly accelerates the wetting trend, while anthropogenic aerosol forcing contributes to drying. Internal variability, particularly the phase transition of Atlantic Multidecadal Variability (AMV), dominates WCAP trends. During the cold-to-warm phase transition of AMV, a barotropic high-pressure system occupied CA as part of the Eurasian Rossby wave train, suppressing local precipitation. This mechanism helps modulate WCAP changes within adaptive ranges. Under high-emission future scenario, the time when WCAP changes exceed these adaptive ranges is projected to occur between 2030 and 2060, at least a decade earlier than under the medium-emission scenario. Considering the importance of WCAP in local agriculture, it is urgent to develop mitigation strategies that limit global warming and delay the time of emergence of significant hydrological impacts.

1. Introduction

Central Asia (CA), one of the world's largest arid and semiarid regions, relies heavily on precipitation as a vital water source for both ecosystems and human livelihoods (Han et al., 2016). However, the region receives sparse annual precipitation, averaging approximately 300 mm, with around 70% concentrated in the spring and winter (Feng et al., 2025; Wang et al., 2022). Global warming has accelerated the hydrological cycle and increased atmospheric water vapor content (Held & Soden, 2006; Oki & Kanae, 2006), prompting numerous studies on precipitation changes in CA (Lioubimtseva & Henebry, 2009; Luo et al., 2019). During the first half of the 20th century, the region experienced a sharp multi-decadal decline in annual precipitation, followed by an increase until the 1980s, particularly in mountainous areas (Hu et al., 2017). Station observations also declare a significant increase in winter Central Asian precipitation (WCAP) at a rate of 0.49 mm year^{-1} between 1960 and 1991 (S.

Writing – review & editing:
Mengyuan Yao, Haosu Tang, Gang Huang

Song & Bai, 2016). Although the general "warming–wetting" trend in CA is projected to intensify under Shared Socio-Economic Pathway 2 and Representative Concentration Pathway 4.5 (SSP2–4.5) future scenario, this does not imply a transition to a "humid climate." Enhanced potential evapotranspiration offsets much of precipitation increases, maintaining the region's arid climate (Yan et al., 2022). While the precipitation intensity is expected to increase significantly under 2°C global warming, limiting warming to 1.5°C could mitigate this intensification (Peng et al., 2019). Although projections show robust increases in long-term WCAP trends under various emission scenarios throughout the 21st century, the number of consecutive dry days is also expected to rise substantially under the high-emission scenario (Zhu et al., 2020). Water resources in arid CA primarily originate from winter snow accumulation and its subsequent spring melt. However, rising temperatures are increasing the likelihood of cold-season precipitation falling as rain rather than snow (Li et al., 2020). Therefore, understanding changes in WCAP may be essential for developing effective strategies to address regional climate change and ensure sustainable water resource management.

The mechanisms driving regional precipitation changes in CA under global warming are highly complex and multifaceted (Yan et al., 2022). The wetting trend observed in eastern CA over the past five decades can be attributed to the human-induced meridional uneven warming pattern, which creates warm advection anomalies and enhances moisture transport through changes in the subtropical westerly jet (SWJ) (Peng et al., 2018). As for individual anthropogenic forcings, rising greenhouse gas emissions favor an equatorial shift of SWJ and increased precipitation over CA (Jiang & Zhou, 2021). In contrast, aerosol emissions generally weaken the SWJ and suppress precipitation over CA (Jiang & Zhou, 2021; F. Song et al., 2014), with sulfate aerosols causing an equatorward shift of the SWJ due to mid-latitude cooling, whereas absorbing black carbon drives a poleward shift of the SWJ (Xie et al., 2022). Moreover, land cover changes also play a role in shaping precipitation changes. Regions with significant vegetation and glacier cover have experienced the most pronounced increases in WCAP due to higher atmospheric water vapor content under elevated temperatures. Conversely, non-vegetated areas have shown only half the precipitation increase observed in vegetated regions (Luo et al., 2019). Additionally, long-term oasis expansion has also enhanced summer precipitation in CA by modifying local land–atmosphere interactions (Cai et al., 2019).

Research indicates that the internal variability of regional precipitation in CA is influenced by various climate patterns. At the interannual timescale, the Pacific Decadal Oscillation (PDO), followed by the Southern Oscillation Index, predominantly explains the primary mode of CA precipitation variability (Yan et al., 2022). Stronger El Niño events favor persistent precipitation anomalies from the mature winter to the decaying summer through large-scale atmospheric convergence and divergence mechanisms (Z. Chen et al., 2022). At the interdecadal timescale, the relationship between CA precipitation and El Niño can be modulated by the horseshoe-like sea surface temperature (SST) anomaly in the North Atlantic, particularly during the rapidly decaying El Niño epoch (M. Yao et al., 2024). Besides, positive phases of tropical Pacific decadal variability could enhance moisture transport to southeastern CA along the northwestern flank of the high sea-level pressure over the Indo–Western Pacific warm pool (Jiang et al., 2021). Additionally, summer precipitation in CA could also be shaped by the Indian Ocean Basin Mode (IOBM), with their relationship further modulated by the Atlantic Multidecadal Variability (AMV). Furthermore, AMV could also serve as a key driver of precipitation anomaly in CA by affecting the amplitude and meridional movement of the SWJ (Wei & Yu, 2024).

Despite previous research on the drivers of precipitation changes in CA, the relative contributions of external forcing and internal variability to WCAP trends remain unclear. This study aims to bridge this knowledge gap by examining the roles of both external forcing and internal variability in shaping inter-decadal WCAP changes. To achieve this, we first disentangle external forcing signals from observed WCAP changes, enabling the reconstruction of internal variability using dominant climate modes. Furthermore, we identify the threshold at which climate change in CA surpasses the region's natural adaptive capacity. This study is guided by three central questions: (a) To what extent do external forcing and internal variability contribute to the inter-decadal variations of WCAP? (b) What are the physical mechanisms driving these inter-decadal variations? (c) When and where will the signals of WCAP changes surpass the background noise of internal variability? By answering these questions, this study attempts to provide a comprehensive understanding of the dynamic interplay between external forcing and internal variability in WCAP changes, offering critical insights for regional climate adaptation and mitigation planning.

2. Data and Methods

2.1. Observational and Model Data

We use the precipitation data from the Global Precipitation Climatology Centre (GPCC) monthly product version 2022 (Schneider et al., 2022), spanning January 1891 to December 2020, to analyze observed changes in the monthly mean of WCAP and to extract its internal variability. To ensure the robustness of the results, we also validate the findings using high-resolution gridded precipitation data sets from the Climatic Research Unit (CRU) (Harris et al., 2020). To verify the reliability of precipitation data sets, we also incorporate daily station observations from the Global Historical Climatology Network (GHCN) (Menne et al., 2012). The total number of rain gauges peaked at over 600 during the 1990s but declined sharply after the dissolution of the Soviet Union in 1991 (Figure S1a in Supporting Information S1). Due to varying record lengths across stations, only those with at least 80% WCAP records are retained to estimate long-term trends. Comparisons of precipitation trends between GPCC and GHCN data sets show high consistency for the periods 1891–2014, pre-1946, and post-1946, confirming the reliability of GPCC data for analyzing WCAP trends, even with limited rain gauge coverage in the early 1900s (Figures S1b–S1d in Supporting Information S1). Meanwhile, the differences in long-term trends between GPCC and CRU are minimal, further validating the robustness of GPCC data. SST data are sourced from the Hadley Centre Sea Ice and SST data set (HadISST) (Rayner et al., 2003). Boreal winter variables are calculated as the seasonal average from December of the current year to February of the following year. Agricultural data, including rice-harvested areas and associated emission values, are derived from the agricultural product consumption and trade data set for the five Central Asian countries, covering the period from 1992 to 2016 (Yang & He, 2019).

We incorporate outputs from 10 climate models, each comprising up to 10 ensemble members, ensuring a balanced analysis with a total of 55 ensemble members (Table S1 in Supporting Information S1). These models are sourced from the Detection and Attribution Model Intercomparison Project (DAMIP) under Phase 6 of the Coupled Model Intercomparison Project (CMIP6) (Gillett et al., 2016). Specifically, the historical simulations include outputs driven by total external forcing, encompassing greenhouse gas (GHG), anthropogenic aerosol (AER), and natural (NAT) forcings. Meanwhile, simulations forced by individual components are analyzed as well to isolate their respective impacts. The historical simulations for each model are designed to reproduce present-day climate conditions from January 1890 to December 2014. For future projections, we employ the SSP2–4.5 and SSP5–8.5 scenarios, which extend the simulations from January 2015 onward. The CMIP6 model outputs analyzed in this study include precipitation, geopotential height, three-dimensional wind fields, and surface temperature. To ensure uniformity, all observations and model simulations are bilinearly interpolated onto a $1° \times 1°$ horizontal grid prior to analysis.

Considering the temporal coverage of both observational data and model outputs, we define the present-day climate as the period from 1891 to 2014 and the climatology as the baseline period from 1901 to 1950. Sensitivity analyses confirm that the main conclusions of this study are robust against variations in the chosen climatological baseline. For future climate projections, we focus on the period from 2015 to 2099 under the SSP scenarios. To ensure continuity in the time series, data for winter 2014 is constructed using December 2014 from the historical simulations and January–February 2015 from the SSP scenarios.

2.2. Rescaled MME

The multi-model ensemble mean (MME) in all-forcing or individual external forcing simulations effectively reduces inter-model uncertainty and offsets internal variability compared to single-model outputs (Deser et al., 2012; Tebaldi & Knutti, 2007). Accordingly, this study assumes that the externally forced response of WCAP is represented by the MME of 55 ensemble members, consistent with previous studies (Deser et al., 2012; Dong et al., 2022; Qin et al., 2020; Risser et al., 2024; Tebaldi & Knutti, 2007). To reconcile the amplitude discrepancies between the model-simulated response and the actual forced response, we first rescale the MME, which represents the externally forced component due to GHG, AER, land use changes, and other external forcings. This rescaling is performed by linearly regressing the MME onto the observed WCAP time series, adjusting the amplitude through the regression intercept. This approach preserves the original shape of the external forcing response while maintaining the integrity of internal variability (Dai et al., 2015; Jeong et al., 2024; Steinman et al., 2015). The rescaling improves the alignment between the MME and observation, reducing the Root Mean Squared Error (RMSE) from 1.84 to 1.58 (Figure 1d). After isolating the externally

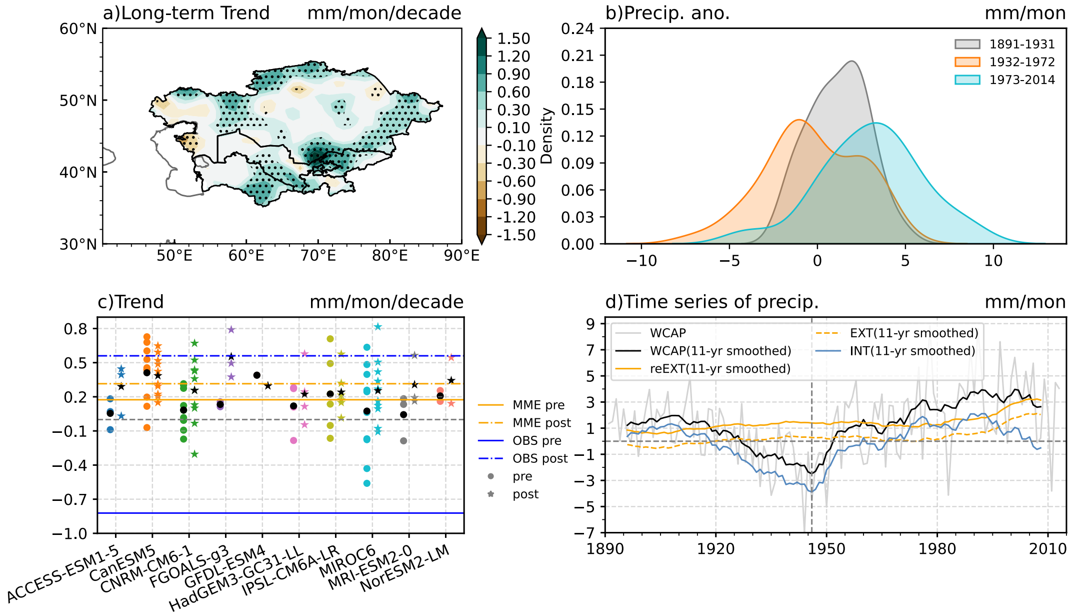

Figure 1. (a) Long-term trend map (unit: mm month^{-1} decade^{-1}) of WCAP in 1891–2014. The dotted regions indicate significance at the 90% level. (b) Probability density function of WCAP anomalies in the period of 1891–1931 (gray), 1932–1972 (orange) and 1973–2014 (blue). (c) Long-term trend (unit: mm month^{-1} decade^{-1}) of WCAP for each member (markers), MME (yellow line) and observation (blue line) in 1891–1946 and 1947–2014. The dots and solid lines represent the earlier period, while the stars and dashed lines correspond to the later period. The colored dots and stars depict the values of individual ensemble members, whereas the black dots and stars indicate the corresponding ensemble mean for each model. (d) Observed WCAP anomaly (unit: mm month^{-1}, gray solid line) and its 11-year running averaged values (unit: mm month^{-1}, black line). The 11-year running averaged externally forced component (unit: mm month^{-1}, yellow dotted line) and its rescaled values (unit: mm month^{-1}, yellow solid line). The 11-year running averaged internally generated component (blue solid line). The vertical gray dashed line indicates the year of 1946.

forced component via the rescaled MME, the internally unforced component, attributed to natural climate variability, is derived by subtracting the rescaled externally forced response from the observed WCAP time series.

To quantify the magnitude of internally generated precipitation variability, we use one standard deviation (1 std.) as the measure, following the established practice in previous literature (Deser et al., 2012; Dong et al., 2022; Qin et al., 2020; Risser et al., 2024; Tebaldi & Knutti, 2007). In the present study, we concentrate on multi-decadal scales by applying an 11-year running average to the areal-weighted regional mean WCAP anomaly time series. The inter-decadal WCAP trend is calculated using a 21-year running trend based on the Theil-Sen Median method, a robust linear regression technique that minimizes the influence of outliers on the trend estimation. To ensure the robustness of the results, alternative window sizes are also tested, including a 9-year running average for smoothing the data and a 19-year running window for trend calculations. The detailed procedure for disentangling externally forced and internally unforced precipitation changes is summarized in the green modules of the flowchart (Figure S2 in Supporting Information S1).

2.3. Climate Mode Index

The monthly AMV index is defined as the detrended winter mean area-averaged SST anomalies over the North Atlantic basin (0°–65°N, 80°W–0°). As proposed by previous studies (Dai et al., 2015; Qin et al., 2020), we also use the surface temperature outputs from historical simulations to separate the external and internal SST signals, with the external signal represented by the MME and the internal signal represented by the residual of the observation from the MME. Thus, the externally forced and internally generated AMV indices can be obtained from the corresponding SST fields, as illustrated by the orange modules of the flowchart (Figure S2 in Supporting Information S1).

The Interdecadal Pacific Oscillation (IPO) index is calculated as the difference between the SST anomalies averaged over the central equatorial Pacific (10°S–10°N, 170°E−90°W) and the average of anomalies in the

Northwest Pacific (25°N–45°N, 140°E−145°W) and Southwest Pacific (50°–15°S, 150°E−160°W). The PDO index is obtained via extracting the principal component of the leading SST pattern through Empirical Orthogonal Function (EOF) analysis at each grid point in the North Pacific basin (polewards of 20°N). The global mean SST have been removed from SST anomalies. To capture low-frequency variability, we apply an 11-year running mean to the monthly indices defined above. Besides, all correlation analyses in this study are conducted using Pearson correlation coefficients.

2.4. Wave-Activity Fluxes

The horizontal wave-activity fluxes are introduced to diagnose the propagation of quasi-stationary Rossby waves (Takaya & Nakamura, 2001), which are defined as:

$$W = \frac{1}{2|\vec{V}|}\begin{cases}\overline{U}\left(\psi_x'^2 - \psi'\psi_{xx}'\right) + \overline{V}\left(\psi_x'\psi_y' - \psi'\psi_{xy}'\right)\\ \overline{U}\left(\psi_x'\psi_y' - \psi'\psi_{xy}'\right) + \overline{V}\left(\psi_y'^2 - \psi'\psi_{yy}'\right)\end{cases} \tag{1}$$

where $\vec{V}$ represents the horizontal wind velocity vector, U and V denote the zonal and meridional wind velocity, respectively. ψ symbolizes the stream function. The primes and overbars signify the regressed anomalies onto the normalized climate mode index and climatological mean-state quantities, respectively.

2.5. Kinetic Energy and Available Potential Energy Conversion

The barotropic energy conversion of kinetic energy (CK) and baroclinic energy conversion of available potential energy (CP) are introduced to diagnose the interactions between perturbations and the background mean flow (Kosaka & Nakamura, 2006), which can be given by:

$$CK = \underbrace{\frac{\left(v'^2 - u'^2\right)}{2}\left(\frac{\partial \overline{u}}{\partial x} - \frac{\partial \overline{v}}{\partial y}\right)}_{CK_x} \underbrace{- u'v'\left(\frac{\partial \overline{u}}{\partial y} + \frac{\partial \overline{v}}{\partial x}\right)}_{CK_y} \tag{2}$$

$$CP = \underbrace{\frac{Rf}{Sp}u't'\frac{\partial \overline{v}}{\partial p}}_{CP_x} \underbrace{- \frac{Rf}{Sp}v't'\frac{\partial \overline{u}}{\partial p}}_{CP_y} \tag{3}$$

where u and v denote the zonal and meridional winds, respectively. Primes and overbars denote the same with Equation 1. R denotes the gas constant, f the Coriolis parameter, $S = (R/p)\left(R\overline{t}/C_p p - d\overline{t}/dp\right)$ denotes the static stability, C_p the specific heat at constant pressure, P the pressure, and t the temperature.

2.6. Time of Emergence

We use the signal-to-noise ratio (SNR) to quantify the relative amplitudes between the climate change signal and natural variability noise, with units of 1 (Hawkins & Sutton, 2012). In this study, the signal is obtained from the temporal average of a 21-year running trend in each ensemble mean, while the noise is calculated as the 1 std. of the observed residual trends, which represent the differences between the observed data and the corresponding model's trends.

The definition of Time of Emergence (ToE) is analogous to SNR. In this context, the signal in ToE is quantified using the rescaled MME of 11-year running-averaged WCAP anomalies, while the noise is determined through two approaches: (a) 1 std. of the internal component, which is derived by subtracting the rescaled MME from the observational data spanning 1891–2014, as previously mentioned; (b) the MME of 1 std. of piControl simulations (any consecutive 500 years) from 10 CMIP6 models. By fixing external forcing at the 1850 level, the piControl simulations can assess the models' internal variability in the absence of changes in external forcing. The ToE is identified as the first year when the signal consistently emerges from the noise and persists through to the end of the 21st century, following the previous definition (Hawkins & Sutton, 2012; Zhang et al., 2024). The SNR and ToE definition procedures are also illustrated in the flowchart for clarity (Figure S2 in Supporting Information S1).

3. Results

3.1. Disentangling External and Internal Components of WCAP Changes

The spatial distribution of mean-state WCAP during the historical period (1891–2014) features relatively higher precipitation in the southeastern mountainous regions (Figure S3a in Supporting Information S1). This spatial pattern is well reproduced by the 10 CMIP6 models used in this study, albeit with slightly larger amplitude in MME (Figures S3a and S3b in Supporting Information S1). The spatial correlation coefficients between each model and the observation all exceed 0.80 (Figure S3c in Supporting Information S1).

A general long-term wetting trend has been observed across CA, with an average increase of 0.23 mm month^{-1} decade^{-1} based on the GPCC data set (Figure 1a). When dividing the historical period (1891–2014) into three equal temporal segments, mean values of WCAP experience a decrease from 1.17 mm month^{-1} in 1891–1931 to −0.26 mm month^{-1} in middle period, followed by a sharp increase to 3.02 mm month^{-1} in 1973–2014 (Figure 1b). Meanwhile, the std. of WCAP increases significantly, from 1.68 mm month^{-1} in the early 20th century to 2.70 mm month^{-1} and 2.89 mm month^{-1} in the middle and late periods, respectively. This widening variability is accompanied by more frequent extreme drought and precipitation events, as well as weakened peak values (Figure 1b).

Decadal precipitation trends exhibit significant variability, characterized by a drying trend of −0.82 mm month^{-1} decade^{-1} before 1946, followed by a wetting trend of 0.56 mm month^{-1} decade^{-1} afterward (Figures 1b and 1c). These trend changes are also corroborated by the GHCN and CRU data sets (Figure S4 in Supporting Information S1). Notably, the CMIP6 MME produces a slightly wetting trend of 0.17 mm month^{-1} decade^{-1} for the period 1891–1946 (Figure 1c). It indicates that the ensemble means of the models may struggle to accurately simulate the observed drying prior to 1946. Nevertheless, several individual model runs successfully replicate the observed drying trend before 1946 and the wetting trend after 1946. This is further supported by the time series and trends of WCAP anomalies in individual runs and their ensemble means (Figure S5 in Supporting Information S1). The limited performance of the MME in capturing early 20th-century drying is partly attributed to the dominant role of internal variability during this period. Since MME largely reflects external forcing, it cancels out much of the internal variability inherent in any single realization (Figure 1c, blue and yellow dotted lines).

The WCAP anomalies are further decomposed into externally forced and internally generated components. Compared to the original external component derived directly from the MME of all-forcing historical simulations, the rescaled external component shows an increase of approximately 1.11 mm month^{-1}, enhancing precipitation response over CA without altering the overall shape. The internal component of observational WCAP closely parallels the 11-year running smoothed observed time series, implying the dominant role of internal variability in observed changes (Figure 1d).

Throughout the study period, WCAP has experienced a wetting trend of 0.23 mm month^{-1} decade^{-1}, driven by external forcing as quantified by the rescaled MME value. This trend is estimated using the Theil-Sen slope within a 21-year running window (Figure S6c in Supporting Information S1). The externally forced wetting trend intensifies after 1946, with an increase of 0.28 mm month^{-1} decade^{-1} compared to 0.19 mm month^{-1} decade^{-1} before 1946. When comparing the internal variability, represented by its 1 std., against the externally forced trend, the internal variability of 1.34 mm month^{-1} decade^{-1} emerges as the dominant factor in determining whether CA becomes wetter or drier (Figure S6 in Supporting Information S1). The increasing precipitation trends attributed to external forcing and the dominant influence of internal variability on WCAP trends remain consistent regardless of the window size or data set used (Figure S6 in Supporting Information S1).

The externally forced precipitation trend can be further decomposed into responses to individual forcings, namely GHG, AER, and NAT forcings. Here, we estimate the response to each forcing directly from the MME of the corresponding historical simulations without applying rescaled adjustments. This is due to the absence of observational responses to individual forcings and the negligible difference in precipitation trends between rescaled and unadjusted estimates. GHG and AER forcings emerge as the dominant drivers of precipitation changes in CA, consistent with previous studies (Jiang & Zhou, 2021; Risser et al., 2024). GHG forcing induces a homogeneous increase in precipitation, with an areal-weighted regional mean wetting trend of 0.21 mm month^{-1} decade^{-1}, ranging from 0.11 to 0.28 mm month^{-1} decade^{-1} as inter-model spread. However, this increase is partially offset by the suppressive effect of AER forcing, which contributes a drying trend of

10.1029/2025EF006064

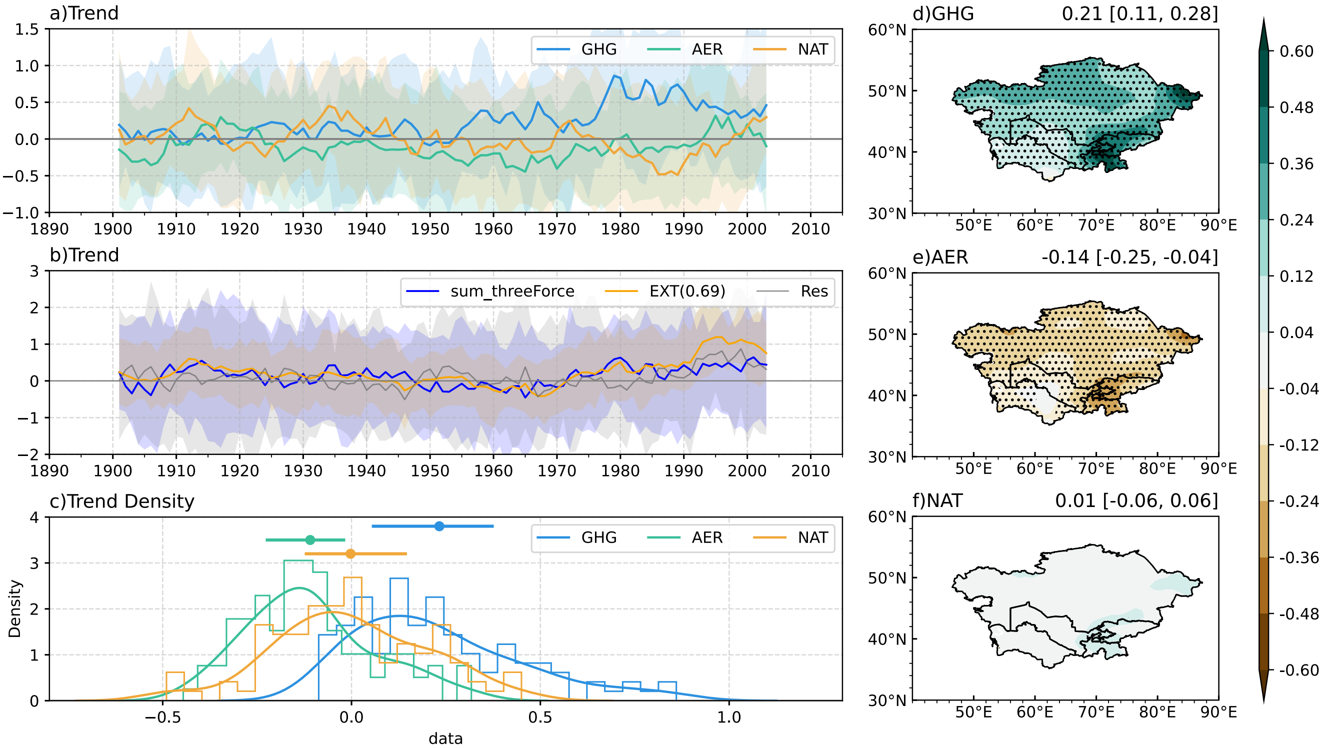

Figure 2. (a) The 21-year running WCAP trends attributed to GHG (unit: mm month^{-1} decade^{-1}, blue), AER (unit: mm month^{-1} decade^{-1}, green), and NAT (unit: mm month^{-1} decade^{-1}, yellow) forcings. The shadings indicate the range of inter-model 25th–75th percentiles. (b) The 21-year running WCAP trend attributed to the sum of three forcings in panel (a) (unit: mm month^{-1} decade^{-1}, dark blue) and total external forcing (unit: mm month^{-1} decade^{-1}, yellow). The residual (unit: mm month^{-1} decade^{-1}, gray) is defined as the difference between total externally forced component and the sum of three individual forcing components. The number in the legend indicates the correlation coefficient between the sum of three individual forcings and total external component. The shadings indicate the range of inter-model 25th–75th percentiles. (c) Generalized extreme value-fitted probability density functions (unit: mm month^{-1} decade^{-1}, curves) and raw histograms (unit: mm month^{-1} decade^{-1}, serrated lines) of 21-year running WCAP trends driven by GHG (blue), AER (green), and NAT (yellow) forcings. The dots and solid lines represent the mean and inter-model 25th–75th percentile range, respectively. (d) The spatial distribution of WCAP trends in 1891–2014 attributed to GHG forcing. The dotted regions indicate significance at the 90% level. The number in the upper right corner indicates the areal-weighted regional mean trend and its 25th–75th percentile range. (e, f) Same as (d), but for AER and NAT forcing, respectively.

−0.14 mm month^{-1} decade^{-1}, with a robust inter-model range of −0.04 to −0.25 mm month^{-1} decade^{-1} (Figures 2a and 2c–2e).

During the historical period, the 200-hPa zonal wind response to GHG forcing was weak in the first half of the 20th century but gradually strengthened in the second half (Figure 3a). Meanwhile, the AER-driven zonal wind response substantially weakened over CA during the mid-to-late 20th century, exhibiting pronounced inter-decadal variability (Figure 3b). The vertically integrated meridional temperature gradient (MTG) provides a clear explanation for the 200-hPa zonal wind changes. Throughout the historical period, the negative MTG induced by GHG forcing amplifies the climatological negative MTG in the mid-latitudes, strengthening and shifting the SWJ southward. This facilitates increased moisture transport to CA (Figures 3c and 3f). In contrast, cooling effects caused by AER forcing weaken the mean-state MTG around CA, leading to the northward shift of SWJ away from CA. It could further decrease moisture transport from oceans and suppress WCAP (Figures 3d and 3f). Here, the intensity and central latitude of SWJ are inferred from the maximum center of 200-hPa zonal wind trends, consistent with previous studies (Ding & Li, 2017; Dong et al., 2022; Lin et al., 2024).

The SWJ response to AER forcing reveals nonlinear changes throughout the historical period (Figure 3f). Before 1946, the southward shift and strengthening of the SWJ associated with AER forcing enhanced WCAP. However, after 1946, the AER-driven SWJ response partially offset the wetting effects of GHG forcing, as a stronger northward shift of the AER-induced SWJ reduced moisture transport to CA, thereby suppressing WCAP (Figure 3f). The mechanisms behind these changes may be traced to the Eurasian industrialization process. From preindustrial times to the mid-20th century, increased European anthropogenic aerosol emissions cooled the

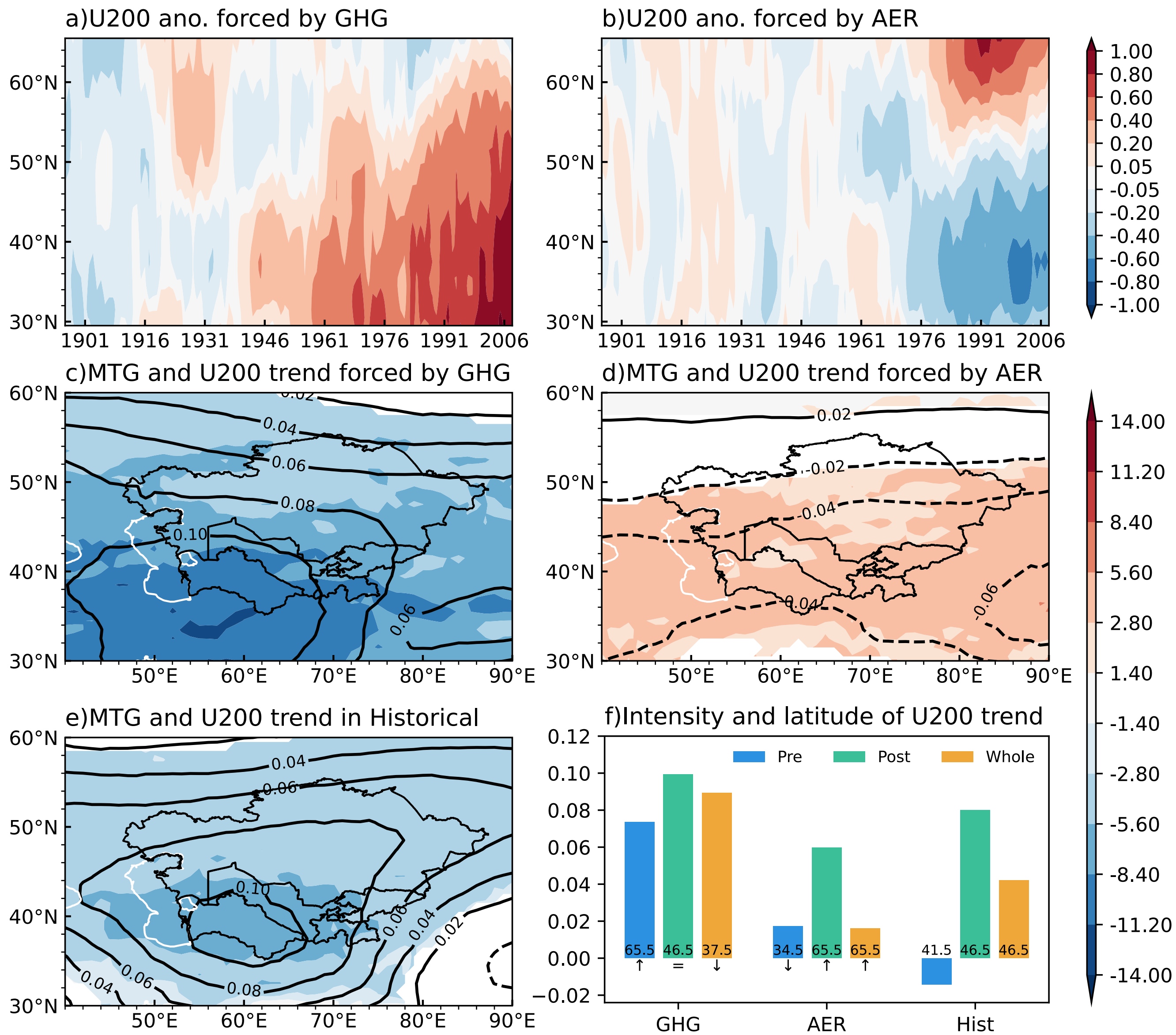

Figure 3. (a) 11-year running averaged 200-hPa zonal wind anomalies averaged from 40° to 90°E driven by GHG forcing (unit: m s^{-1}, shading) in 1891–2014. The climatology is defined as the mean over the period from 1901 to 1950. (b) Same as (a), but for AER forcing. (c) The 200-hPa zonal wind trend (unit: m s^{-1} $decade^{-1}$, contour) and vertically integrated MTG trend ($-\frac{\partial T}{\partial y}$, unit: 10^{-6} K $decade^{-1}$ m^{-1} hPa^{-1}, shading) attributed to GHG forcing in 1891–2014. The shading values are shown only above 90% significance level. (d, e) Same as (c), but for AER and all forcing, respectively. (f) The averaged intensify (unit: m s^{-1} $decade^{-1}$, bar) and latitude (unit: degree, number) of maximum 200-hPa zonal wind trends from 40°E to 90°E before 1946 (blue), after 1946 (green) and in the whole period of 1891–2014 (yellow) attributed to GHG, AER, and all forcing simulations. The upward and downward arrows (or equal sign) represent the northward and southward (or stationary) displacement of the subtropical westerly jet relative to that in the historical simulation, respectively.

Atlantic–Eurasian region, intensifying the climatological MTG across mid-latitude Eurasia (Undorf et al., 2018). This intensified MTG caused a southward shift of the SWJ, enhancing WCAP. However, after the mid-20th century, reductions in aerosol emissions in Europe, coupled with increased emissions from lower-latitude regions such as East and South Asia, reversed this trend. These shifts weakened the mean-state MTG over CA, driving the SWJ northward and reducing WCAP (Dong et al., 2022; Undorf et al., 2018).

The NAT forcing exerts little effect on the WCAP trend, contributing an average of only 0.01 mm $month^{-1}$ $decade^{-1}$ during the whole period, with an inter-model range spanning from −0.06 to 0.06 mm $month^{-1}$ $decade^{-1}$ (Figures 2a and 2f). However, a pronounced precipitation reduction attributed to NAT forcing occurred between 1985 and 1990, likely driven by consecutive volcanic eruptions during the 1980s, such as the El Chichón eruption in 1982 and the Kliuchevskoi eruptions from 1984 to 1987, which may favor drier conditions in CA (Anchukaitis, 2012; Man et al., 2014). The overall externally forced precipitation trends can be well captured by the sum of the individual components driven by GHG, AER, and NAT forcings, with a significant correlation coefficient of 0.64 (Figure 2b). The residual, defined as the difference between the total externally forced component and the combined contributions of three individual forcings, remains close to zero for most of the study period, except after the 1990s. This anomalous rise in residuals may be attributed to significant land use and land cover changes in CA during 1990–2009 (X. Chen et al., 2013). Following the collapse of the Soviet Union in 1991, extensive areas of abandoned farmland were converted back to natural vegetation (Lioubimtseva et al., 2005), altering the landscape and intensifying the hydrological cycle in the region.

The generalized extreme value (GEV)-fitted probability density functions, along with raw histograms of 21-year running trends for the three single-forcing components, are shown in Figure 2c. These results indicate that the GHG-driven increase in WCAP can reach up to 1.00 mm month^{-1} decade^{-1}, significantly exceeding the AER-induced decrease of -0.5 mm month^{-1} decade^{-1}. The bell curve for NAT forcing is nearly symmetric around zero, reflecting its oscillatory effect on precipitation with year-to-year fluctuations (Figure 2c). Similar findings could be obtained when the curves are fitted using Gaussian distributions or kernel density estimators.

3.2. Influence of Internal Variability on WCAP Changes

In the previous sub-section, we decompose the observed WCAP time series into externally forced and internally generated components. The externally forced component is further disaggregated into three individual forcing components. In this sub-section, we investigate the extent to which internal variability can be attributed to major multi-decadal climate modes, including AMV, PDO, and IPO.

High levels of internal variability are primarily located around the margins of deserts in central CA, while lower values are concentrated within desert areas (Figure 4a). Among the climate modes examined, AMV stands out with a significant negative correlation coefficient of -0.74 ($p < 0.001$), whereas IPO and PDO exhibit statistically insignificant correlations. Notably, not only does the spatially averaged internal component of WCAP correlate strongly with AMV, but this relationship is also consistent across individual grid points (Figure 4b). Further Pearson correlation analysis indicates that the positive phase of AMV is significantly associated with suppressed WCAP, accompanied by anomalous subsidence across most of CA, except for western and southeastern edge regions (Figures 4c and 4d). Consequently, AMV is identified as the primary factor to regress the internal component.

The AMV has undergone three phase transitions since early 20th century: a negative-to-positive transition around 1925, a positive-to-negative transition around 1966, and another negative-to-positive transition around 1997 (Figure 4e). The cold-to-warm AMV phase shift induces a decreasing WCAP trend of -0.39 mm month^{-1} decade^{-1}, with values declining from -0.09 to -1.22 mm month^{-1} between 1891 and 1946. Conversely, the warm-to-cold AMV phase transition from 1947 to 1997 leads to an increasing WCAP trend of 0.90 mm month^{-1} decade^{-1}, with values rising from -1.49 to 0.22 mm month^{-1} (Figure 4e). Prior to regression, we normalize the AMV index and smooth all variables using an 11-year running average. The reconstructed internal component effectively captures the variance of observed internal variability, with a goodness-of-fit of 0.55 and an error bias of 1.06. However, it slightly underestimates the amplitude of the sharp decline between 1930 and 1950 (Figure 4e). Additionally, the WCAP anomaly time series (black line in Figure 4e), reconstructed by combining the rescaled externally forced component and the reconstructed internal component, exhibits a strong correlation with observations, with a correlation coefficient of 0.78. The reconstruction reveals a decreasing trend of -0.20 mm month^{-1} decade^{-1} before 1946, followed by an increasing trend of 0.99 mm month^{-1} decade^{-1} afterward.

Furthermore, we isolate the unforced natural component of AMV by subtracting the externally forced MME of AMV from the observed AMV index. This unforced component is applied to the reconstruction as well, achieving a goodness-of-fit of 0.54 and an error bias of 1.07 (Figure 4f). Its performance closely aligns with that of the original AMV index (Figure 4e), indicating that the influence of AMV on WCAP may primarily be driven by internal variability rather than external forcing. This conclusion is also supported by the negligible difference between AMV and its internal component, except after the 2000s, when anthropogenic impacts became more pronounced (Figures 4e and 4f).

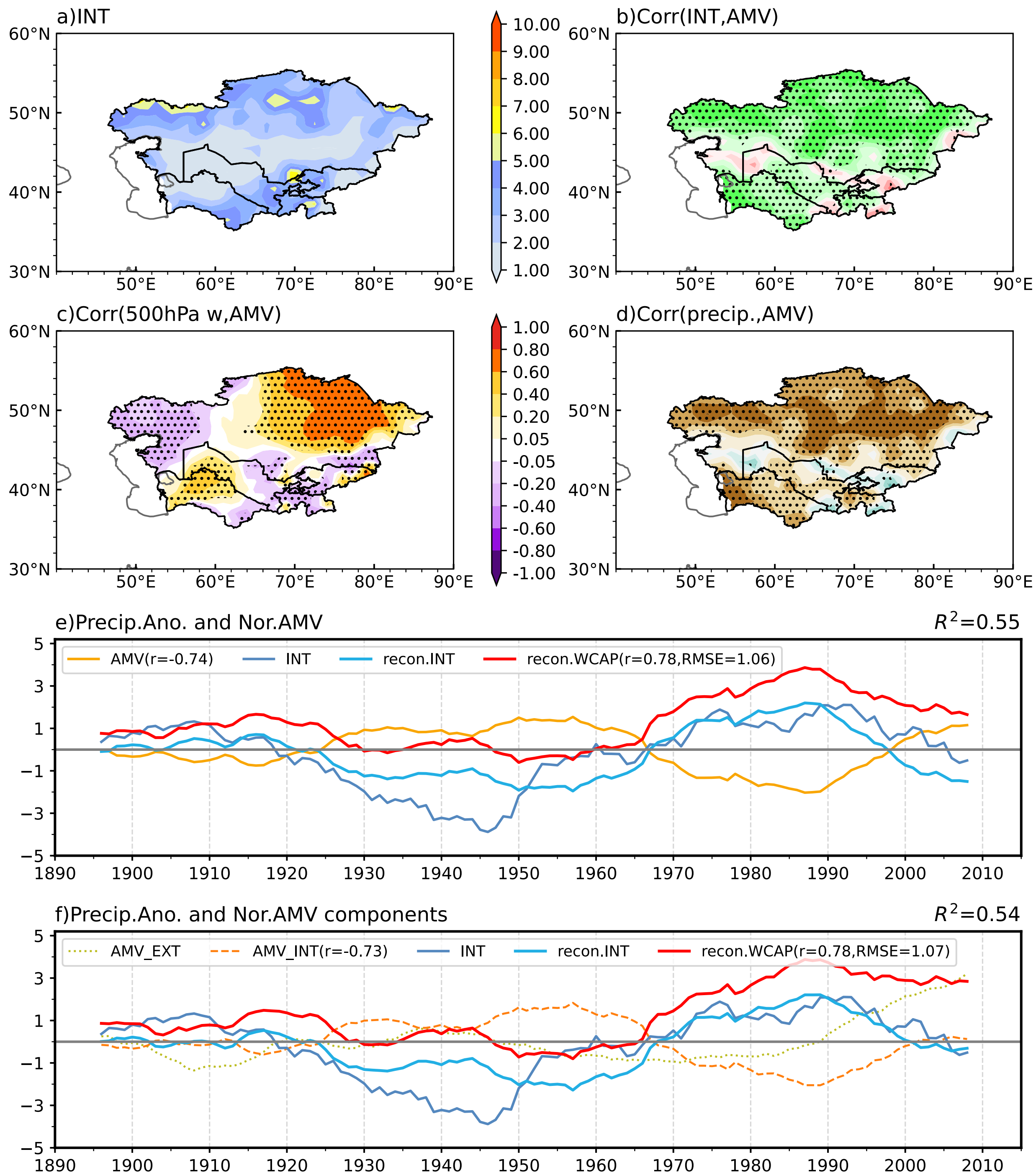

Figure 4. (a) One standard deviation for the internal component of the WCAP changes (unit: mm month^{-1} decade^{-1}). (b) Correlation of internal component of WCAP anomalies and AMV index at each grid over CA. The dotted regions indicate significance at the 90% level. (c, d) Same as (b), but for 500-hPa vertical pressure velocity and precipitation, respectively. (e) Time series of AMV index (yellow line) and internally generated component of WCAP anomalies in the observation (dark blue). AMV-based reconstructed time series of internally generated component (light blue) and WCAP anomalies (red line). The numbers in the left legend and at upper right corner indicate the correlation coefficient and goodness-of-fit (square correlation) between AMV and internally generated component of observed WCAP anomalies, respectively. The number in the right legend indicates the correlation coefficient and RMSE of WCAP between in observation and reconstruction. (f) Same as (e), but AMV is furtherly separated into externally forced (AMV_EXT) and internal (AMV_INT) components. The reconstruction of internally generated component (light blue) and WCAP anomalies (red line) is based on the AMV_INT. All variables are averaged at 11-year running window.

10.1029/2025EF006064

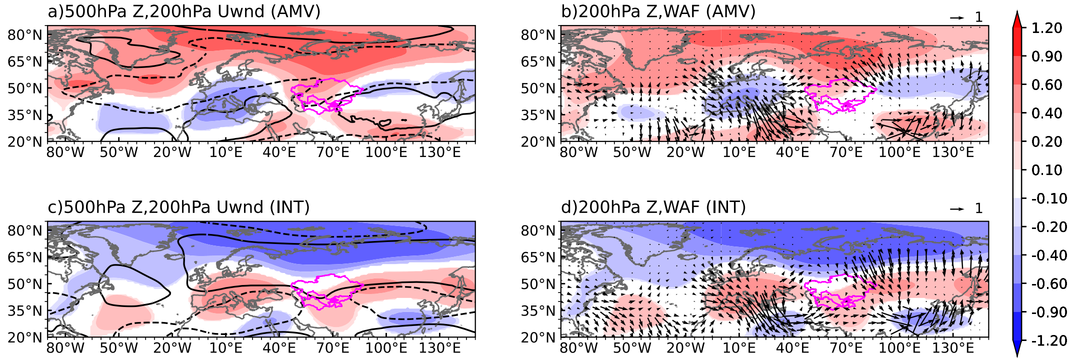

Figure 5. (a) Regression of 500-hPa geopotential height (unit: m, shading) and 200-hPa zonal wind (unit: m s^{-1}, contour, only value of ±0.25 is shown) against AMV index. (b) Regression of 200-hPa geopotential height (unit: m, shading) against AMV index, and the corresponding wave activity flux (unit: m^2 s^{-2}, vector). The shading and vector values are shown only above 90% significance level. (c, d) Same as (a, b), but for regression against INT. All variables are averaged at 11-year running window.

We further investigate the dynamic mechanisms underlying the remote control of AMV phase transition on WCAP trends. Figures 5a and 5b illustrate an eastward-propagating barotropic Rossby wave train initiated by AMV, originating from the subtropical Atlantic. This wave train propagates along the Eurasian westerly jet stream, then splitting into two branches upon encountering the continents. One branch continues eastward toward CA, while the other propagates southeastward toward North Africa and the Red Sea. The barotropic high-pressure system occupying over CA leads to a reduction in WCAP, consistent with previous results (Figures 4c and 4d). The regression on the internal component shares a similar origin and propagation path for the wave train as observed in the regression with AMV index (Figure 5). This indicates that the Rossby wave train induced by AMV may play a significant role in shaping CA's atmospheric circulation anomalies and modulating the internal variability of WCAP.

To further investigate the maintenance mechanisms of this Eurasian Rossby wave train, we analyze regressions of vertically integrated kinetic energy and available potential energy conversion against internal variability

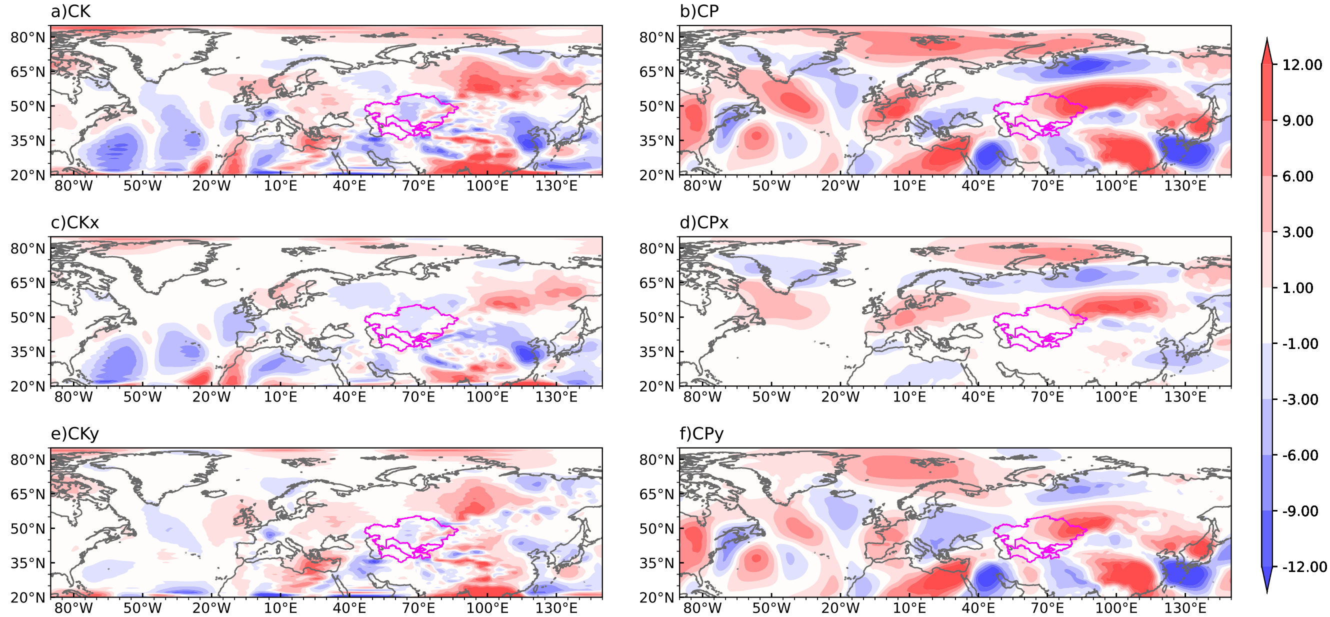

Figure 6. (a) Regression of vertically integrated conversion of kinetic energy (unit: W m^{-2}) against INT. (c, e) Same as (a), but for its zonal and meridional components, respectively. (b, d, f) Same as (a, c, e), bur for available potential energy and its zonal and meridional components (unit: W m^{-2}), respectively. All variables are averaged at 11-year running window.

(Figure 6). The most prominent *CP* over the Atlantic aligns with the origin of the wave train. East of the prime meridian, *CP* values alternate between positive and negative along the SWJ, with positive anomalies over North Africa and Afghanistan, and negative anomalies over Saudi Arabia and North India (Figures 5c and 6b). The dominant contribution to *CP* comes from its meridional component, which significantly supplies the baroclinic energy necessary to sustain the wave train. In contrast, the contribution of *CK*, primarily from its zonal component, is minimal and could largely be disregarded (Figure 6). Notably, the net energy gain along the wave train's propagation path exceeds the energy loss, implying that the wave train effectively extracts energy from the background mean flow. The barotropic high-pressure system over CA, as part of the Rossby wave train induced by AMV, could be maintained by the energy sourced from the background SWJ. This persistent system suppresses WCAP during the cold-to-warm phase transition of AMV, providing a mechanistic explanation for the observed precipitation trends.

3.3. Future Projections and Time of Emergence

The above analysis has elaborated on the contributions of individual forcing and internal variability to WCAP changes during the historical period (1891–2014). Building on this, we extend the analytical framework to future projections (2015–2099), exploring the sensitivity of WCAP trends to varying emission scenarios across different models and time periods.

Precipitation trends exhibit notable variability among models in the all-forcing historical simulations, with externally forced 21-year running WCAP trends ranging from 0.13 to 0.44 mm month^{-1} decade^{-1}. These simulated trends align well with the observation, demonstrating that the models effectively capture historical precipitation changes (Figure 7a). When comparing historical outputs with projections under two future emission scenarios, the MME wetting trend strengthens with increasing greenhouse gas emission intensity. The widest range and maximum MME values are observed under the SSP5–8.5 scenario, with trends ranging from 0.71 to 2.48 mm month^{-1} decade^{-1}. This suggests that intensified greenhouse gas emissions not only amplify WCAP wetting trends but also introduce greater uncertainties (Figure 7a). Under the SSP5–8.5 scenario, the projected wetting trends are nearly four times higher than those in the historical simulations and twice as high as those under the SSP2–4.5 scenario, highlighting the substantial impact of emission pathways on future WCAP changes (Figure 7a).

The variance in precipitation variability is further assessed across three scenarios reflecting natural adaptive capacity (Figure 7b). While MME and trend ranges are relatively consistent across scenarios, the SSP5–8.5 scenario exhibits slightly larger variability, with the 1 std. of 21-year running WCAP internal trends in the temporal dimension ranging from 0.53 to 1.85 mm month^{-1} decade^{-1} (Figure 7b). To assess the relative amplitude of externally forced responses versus internal variability, the SNR of 21-year running WCAP trends is further used as an indicator. In the historical simulation, internal variability generally obscures the externally forced response, with no model achieving an SNR greater than 1. However, in future projections, both the trend signal and SNR increase, particularly under the SSP5–8.5 scenario, where the MME SNR reaches up to 1.22. This highlights the increasing dominance of externally forced changes and the growing likelihood that inter-decadal trends driven by anthropogenic climate change will surpass the natural variability range in the future (Figure 7c).

The ToE marks the point at which the SNR of the 11-year running WCAP anomalies consistently exceeds 1, indicating that the wetting signal has emerged from the internal noise. This also implies that natural regulation can no longer reverse the external effects of climate change on WCAP. Compared to SNR, ToE provides a more intuitive reference for understanding when externally forced wetting trends break through natural variability. The regional averaged ToE for CA is identified as 2018 for the SSP2–4.5 scenario and 2015 for the SSP5–8.5 scenario (Figure 7d). The relative contributions of external forcing in both scenarios increase sharply in the late twentieth century, with a particularly strong impact on the wetting trend under the SSP5–8.5 scenario.

Excluding the regions of southwestern CA, where the ToE has already occurred before 2010, the ToE mainly occurs after the 2060s under the SSP2–4.5 scenario. In contrast, under the SSP5–8.5 scenario, the ToE is projected to occur between 2040 and 2060 in central CA and as early as the 2030s in eastern CA, with at least a decade's difference between the two scenarios (Figures 7e and 7f). Note that the areal-averaged ToE signal may be somewhat advanced by the climate changes that have already occurred before 2010, which leads to a less pronounced contrast in regional mean results between the two scenarios (Figure 7d). The earlier ToE in the SSP5–8.5 scenario highlights the accelerated influence of high-emission pathways, resulting in the earlier breaching of the

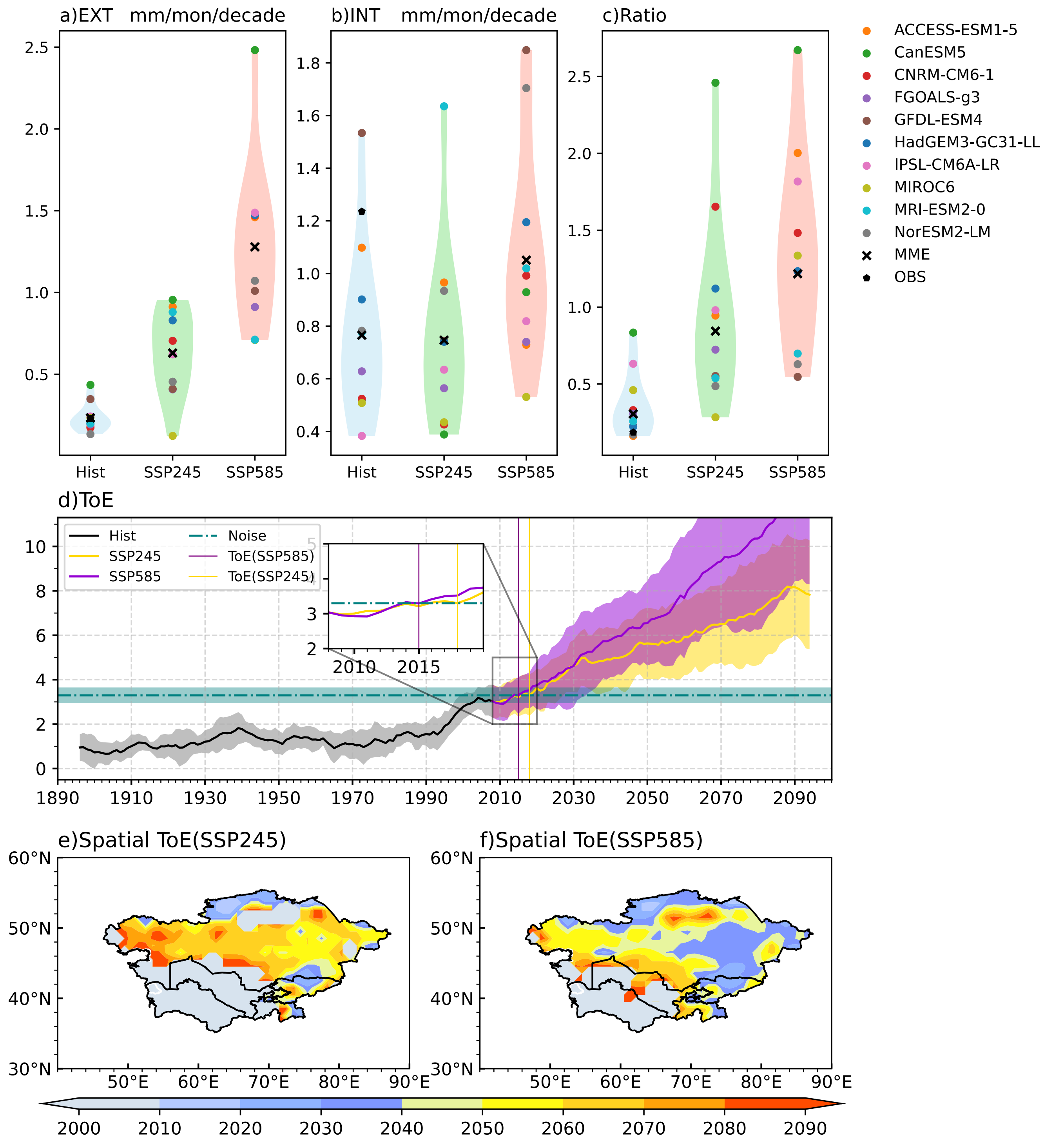

Figure 7. (a) The violin and scatter plot of 21-year running externally forced WCAP trends (unit: mm month^{-1} decade^{-1}) for each model, MME and observation in historical simulations (1891–2014), SSP2–4.5 (2015–2099), and SSP5–8.5 (2015–2099) scenarios. (b, c) Same as (a), but for one standard deviation (unit: mm month^{-1} decade^{-1}) and the ratio between panels (a) and (b). (d) The 11-year running averaged time series of externally forced WCAP anomalies (unit: mm) in historical simulations (black), SSP2–4.5 (yellow) and SSP5–8.5 (purple) scenarios. The shadings indicate the corresponding one standard deviation among models. The inset figure is to clarify the ToE. The yellow and purple vertical lines for SSP2–4.5 and SSP5–8.5 scenarios indicate year of 2018 and 2015, respectively. (e) The spatial distribution of ToE under SSP2–4.5 scenario at each grid over CA. (f) Same as (e), but under SSP5–8.5 scenario.

natural variability boundaries by external climate change (Abatzoglou et al., 2019; Lyu et al., 2014; Williams et al., 2024). In other words, the delayed ToE in the SSP2–4.5 scenario underscores the role of emission reductions in mitigating the impacts of climate change (S. Chen et al., 2024).

Similar ToE results could be obtained when the internal noise is calculated using piControl simulations (Figure S7 in Supporting Information S1). Besides, the sensitive analysis of various SNR thresholds to determine ToE is also conducted (Figure S7d in Supporting Information S1). As the SNR thresholds increase, the external forcing response faces greater difficulty in emerging from the internal variability. This results in a slower emergence of severer risks and a delayed ToE across CA, shifting from the 2030s to post-2060. Notably, using a SNR of 2 to identify ToE of WCAP may be unreasonable, as it causes a slower exposure of the entire CA under the high-emission scenario compared to the medium-emission scenario, which is inconsistent with actual projections (Figure S7d in Supporting Information S1).

4. Summary and Discussion

In this study, the WCAP trend has been decomposed into the externally forced trend and internal component whose 1 std. represents the multi-decadal variability of WCAP. The rescaled external component, derived from the MME of 55 CMIP6 ensemble members, exhibits a consistent increasing trend in WCAP, peaking after the 2000s. This finding indicates that external forcing generally favors increased WCAP over the historical period. Further decomposition of external forcing into GHG, AER, and NAT forcings reveals that GHG forcing predominantly drives the wetting trend. This influence of GHG forcing primarily manifests through the southward shift of the SWJ and enhanced moisture transport throughout the historical period, effectively counteracting the drying effect caused by AER forcing. The contribution of NAT forcing is negligible, with an average effect close to zero over the long term.

The internal variability component of the WCAP trend is more pronounced than its external forcing counterpart. Specifically, the standard deviation of internal variability (1.34 mm $month^{-1}$ $decade^{-1}$) significantly outweighs the average trend of the external component (0.23 mm $month^{-1}$ $decade^{-1}$). This internal variability can be well reconstructed by AMV, which exhibits a strong negative correlation with WCAP anomalies. The cold-to-warm AMV phase transition from 1891 to 1946 suppressed the externally forced upward precipitation trend, reversing it from 0.19 to −0.20 mm $month^{-1}$ $decade^{-1}$, which contributed to the drying trends over CA observed before 1946. In contrast, the subsequent warm-to-cold AMV phase shift from 1947 to 1997 amplified the externally forced precipitation trend, increasing it from 0.28 to 0.99 mm $month^{-1}$ $decade^{-1}$, resulting in a pronounced wetting trend. From a dynamic perspective, the positive phase of the AMV can trigger a Rossby wave train that suppresses precipitation in CA by establishing a barotropic high-pressure system. This eastward-propagating wave train along the Eurasian westerly jet is sustained through baroclinic energy extraction from the background mean flow. The mechanisms underlying the externally forced and internally generated changes in WCAP are summarized in Figure 8.

Future climate projections under the SSP2–4.5 and SSP5–8.5 scenarios indicate a substantial increase in the influence of external forcing on WCAP wetting trends, while the role of internal variability is expected to remain relatively stable. Notably, only under the SSP5–8.5 scenario does the MME SNR during the period 2015–2099 exceed 1. This indicates more severe and urgent climate risks, as the stronger wetting trends driven by external forcing in high-emission scenarios exert a greater modulation on WCAP than natural variability. In other words, the ToE, the point at which precipitation changes driven by external forcing surpass the range of natural climate variability and self-adaptation, occurs at least a decade earlier in scenarios with higher carbon dioxide emissions. Specifically, under the SSP5–8.5 scenario, the ToE is projected to occur in the 2030s over eastern CA and between 2040 and 2060 over central CA. In contrast, under the SSP2–4.5 scenario, the ToE is expected to occur after 2060.

As a global "breadbasket" producing rice, wheat, and maize (Swinnen et al., 2017; Yu et al., 2020), WCAP plays a crucial role in sustaining agricultural productivity and ensuring food security across the world. Here, we further find that the internal variability of WCAP may serve as an indicator of local rice cultivation, including harvested area and associated emissions (measured as carbon dioxide equivalent), for both the current and subsequent years. These relationships are evidenced by significant correlation coefficients of 0.74 and 0.77 ($p < 0.05$), respectively. Among the five CA countries, the strongest indicator relationships are observed in Kazakhstan and Uzbekistan. This finding highlights the potential utility of AMV, which can effectively reconstruct WCAP's internal

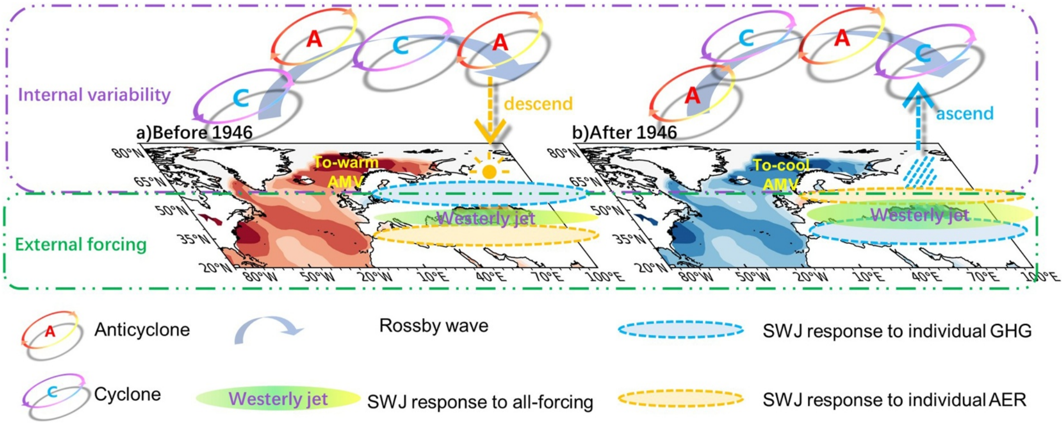

Figure 8. Schematic diagram illustrating the underlying mechanisms driving drying and wetting conditions over CA (a) before and (b) after 1946. The diagram includes position changes of subtropical westerly jet (SWJ), phase transition of AMV, precipitation trends over CA and the 200-hPa Rossby wave train induced by the AMV phase transition. Red (blue) shadings in the North Atlantic indicate cold-to-warm (warm-to-cold) phase transition of AMV. Blue curves indicate the Rossby wave train paths. The letter A (C) indicates atmospheric anticyclone (cyclone) anomalies. Green shading, blue dashed and yellow dashed ovals denote the SWJ responses to all-forcing, individual GHG and AER forcing, respectively. Yellow sun symbol and downward arrow over CA denote drying conditions and anomalous descending trends, respectively. Blue rain symbol and upward arrow over CA denote wetting conditions and anomalous ascending trends, respectively.

variability, for improving grain cultivation and storage predictions in CA. Future studies could delve deeper into the integration of AMV-driven internal variability with agricultural planning models to bolster the resilience of agricultural production systems under changing climatic conditions.

The external forcing and internal variability disentanglement framework applied to WCAP in this study can also be extended to other regions and climate variables that are closely tied to human livelihoods. For instance, it could be applied to investigate precipitation changes in other semi-arid or monsoon regions, or to analyze trends in temperature extremes or drought severity. A concrete example is the increasing wildfire risk in the southwestern United States, which is influenced by a combination of external forcings (e.g., greenhouse gas emissions) and large-scale climate drivers (e.g., PDO). By applying this framework, it is possible to quantitatively assess how the regional fire weather index responds to both human-induced climate change and natural variability, providing a more comprehensive understanding of its long-term dynamics. Moreover, this framework provides valuable insights for climate risk assessments by pinpointing regions and timeframes where externally forced changes surpass the bounds of internal variability. This can help identify the timing and magnitude of emerging climate risks, enabling more targeted adaptation and mitigation strategies. By highlighting when and where the climate system may exceed its natural variability, this framework may support proactive decision-making to reduce vulnerabilities and enhance resilience to future climate change impacts. Notably, rescaling model outputs may be a necessary prerequisite for reliable signal separation, given that CMIP6 models not only inadequately represent internal variability but also exhibit systematic biases. For instance, CMIP models generally underestimate both total winter wet-day precipitation and extreme precipitation trends over CA (Liu et al., 2022; J. Yao & Chen, 2015). In the present study, models with greater dry biases tend to simulate less pronounced wetting trends than observed (Figure S8 in Supporting Information S1). These biases can potentially distort the estimation of the forced signal, highlighting the importance of bias adjustment to ensure the robustness of attribution results (Figure 1 and Figure S5 in Supporting Information S1).

In the present study, AMV has been identified as the key factor influencing the internal variability of WCAP, with its influence likely to persist over the coming decades. This finding underscores the potential of leveraging AMV to effectively reduce uncertainty in near-term projections of WCAP. Incorporating potential AMV phase transitions into climate models could provide a more accurate projection of future precipitation trends in the region, thereby enhancing predictive capabilities. To build on these insights, future research could focus on developing methodologies that integrate AMV signals with other climate drivers to refine projections and better inform adaptation strategies for water resource management in CA.

Conflict of Interest

The authors declare no conflicts of interest relevant to this study.

Data Availability Statement

All the data that support the findings are free for open access. Monthly precipitation data are available from Schneider et al. (2022) and Harris et al. (2020). HadISST data set is sourced from Met Office Hadley Center (Rayner et al., 2003). Observed stational precipitation data of GHCN is available from Menne et al. (2012). CMIP6 data sets archived in DAMIP could be accessible from Gillett et al. (2016) (see details in Table S1 in the Supporting Information S1). The agricultural product data in CA are accessible from National Tibetan Plateau/Third Pole Environment Data Center (Yang & He, 2019).

Acknowledgments

We sincerely appreciate the associate editor and anonymous reviewers for their insightful comments, which have significantly enhanced the quality of this manuscript. Besides, we are indebted to the World Climate Research Programme (WCRP)'s Working Group on Coupled Modeling and extend our gratitude to the climate modeling groups worldwide (listed in Table S1 in Supporting Information S1) for their efforts in producing and making their model outputs publicly available. This work is funded by the National Natural Science Foundation of China (42141019 and 42261144687).

References

Abatzoglou, J. T., Williams, A. P., & Barbero, R. (2019). Global emergence of anthropogenic climate change in fire weather indices. *Geophysical Research Letters*, *46*(1), 326–336. https://doi.org/10.1029/2018GL080959

Anchukaitis, K. J., Breitenmoser, P., Briffa, K. R., Buchwal, A., Büntgen, U., Cook, E. R., et al. (2012). Tree rings and volcanic cooling. *Nature Geoscience*, *5*(12), 836–837. https://doi.org/10.1038/ngeo1645

Cai, P., Hamdi, R., Luo, G., He, H., Zhang, M., Termonia, P., & De Maeyer, P. (2019). Agriculture intensification increases summer precipitation in Tianshan Mountains, China. *Atmospheric Research*, *227*, 140–146. https://doi.org/10.1016/j.atmosres.2019.05.005

Chen, S., Yuan, X., Ma, Y., Zhuang, Q., & Shurpali, N. J. (2024). The timing of detectable increases in seasonal soil moisture droughts under future climate change. *Earth's Future*, *12*(6), e2023EF004330. https://doi.org/10.1029/2023ef004174

Chen, X., Bai, J., Li, X., Luo, G., Li, J., & Li, B. L. (2013). Changes in land use/land cover and ecosystem services in Central Asia during 1990–2009. *Current Opinion in Environmental Sustainability*, *5*(1), 116–127. https://doi.org/10.1016/j.cosust.2012.12.005

Chen, Z., Wu, R., Zhao, Y., & Wang, Z. (2022). Different responses of Central Asian precipitation to strong and weak El Niño Events. *Journal of Climate*, *35*(5), 1497–1514. https://doi.org/10.1175/jcli-d-21-0238.1

Dai, A., Fyfe, J. C., Xie, S.-P., & Dai, X. (2015). Decadal modulation of global surface temperature by internal climate variability. *Nature Climate Change*, *5*(6), 555–559. https://doi.org/10.1038/nclimate2605

Deser, C., Phillips, A., Bourdette, V., & Teng, H. (2012). Uncertainty in climate change projections: The role of internal variability. *Climate Dynamics*, *38*(3), 527–546. https://doi.org/10.1007/s00382-010-0977-x

Ding, F., & Li, C. (2017). Subtropical westerly jet waveguide and winter persistent heavy rainfall in south China. *Journal of Geophysical Research: Atmospheres*, *122*(14), 7385–7400. https://doi.org/10.1002/2017JD026530

Dong, B., Sutton, R. T., Shaffrey, L., & Harvey, B. (2022). Recent decadal weakening of the summer Eurasian westerly jet attributable to anthropogenic aerosol emissions. *Nature Communications*, *13*(1), 1148. https://doi.org/10.1038/s41467-022-28816-5

Feng, K., Cao, Y., Du, E., Zhou, Z., & Zhang, Y. (2025). Spatiotemporal dynamics of drought and the ecohydrological response in Central Asia. *Remote Sensing*, *17*(1), 166. https://doi.org/10.3390/rs17010166

Gillett, N. P., Shiogama, H., Funke, B., Hegerl, G., Knutti, R., Matthes, K., et al. (2016). The detection and attribution model Intercomparison Project (DAMIP v1.0) contribution to CMIP6 [Dataset]. *Geoscientific Model Development*, *9*(10), 3685–3697. https://doi.org/10.5194/gmd-9-3685-2016

Han, Q., Luo, G., Li, C., Shakir, A., Wu, M., & Saidov, A. (2016). Simulated grazing effects on carbon emission in Central Asia. *Agricultural and Forest Meteorology*, *216*, 203–214. https://doi.org/10.1016/j.agrformet.2015.10.007

Harris, I., Osborn, T. J., Jones, P., & Lister, D. (2020). Version 4 of the CRU TS monthly high-resolution gridded multivariate climate dataset [Dataset]. *Scientific Data*, *7*(1), 109. https://doi.org/10.1038/s41597-020-0453-3

Hawkins, E., & Sutton, R. (2012). Time of emergence of climate signals. *Geophysical Research Letters*, *39*(1), L01702. https://doi.org/10.1029/2011gl050087

Held, I. M., & Soden, B. J. (2006). Robust responses of the hydrological cycle to global warming. *Journal of Climate*, *19*(21), 5686–5699. https://doi.org/10.1175/JCLI3990.1

Hu, Z.-Y., Zhou, Q., Chen, X., Qian, C., Wang, S., & Li, J. (2017). Variations and changes of annual precipitation in Central Asia over the last century. *International Journal of Climatology*, *37*(S1), 157–170. https://doi.org/10.1002/joc.4988

Jeong, D., Yoo, C., & Yeh, S.-W. (2024). Contributions of external forcing and internal variability to the multidecadal warming rate of East Asia in the present and future climate. *npj Climate and Atmospheric Science*, *7*(1), 22. https://doi.org/10.1038/s41612-024-00573-w

Jiang, J., & Zhou, T. (2021). Human-induced rainfall reduction in drought-prone northern Central Asia. *Geophysical Research Letters*, *48*(7), e2020GL092156. https://doi.org/10.1029/2020gl092156

Jiang, J., Zhou, T., Chen, X., & Wu, B. (2021). Central Asian precipitation shaped by the tropical Pacific decadal variability and the Atlantic Multidecadal Variability. *Journal of Climate*, *34*(18), 7541–7553. https://doi.org/10.1175/jcli-d-20-0905.1

Kosaka, Y., & Nakamura, H. (2006). Structure and dynamics of the summertime Pacific–Japan teleconnection pattern. *Quarterly Journal of the Royal Meteorological Society*, *132*(619), 2009–2030. https://doi.org/10.1256/qj.05.204

Li, Z., Chen, Y., Li, Y., & Wang, Y. (2020). Declining snowfall fraction in the alpine regions, Central Asia. *Scientific Reports*, *10*(1), 3476. https://doi.org/10.1038/s41598-020-60303-z

Lin, L., Hu, C., Wang, B., Wu, R., Wu, Z., Yang, S., et al. (2024). Atlantic origin of the increasing Asian westerly jet interannual variability. *Nature Communications*, *15*(1), 2155. https://doi.org/10.1038/s41467-024-46543-x

Lioubimtseva, E., Cole, R., Adams, J. M., & Kapustin, G. (2005). Impacts of climate and land-cover changes in arid lands of Central Asia. *Journal of Arid Environments*, *62*(2), 285–308. https://doi.org/10.1016/j.jaridenv.2004.11.005

Lioubimtseva, E., & Henebry, G. M. (2009). Climate and environmental change in arid Central Asia: Impacts, vulnerability, and adaptations. *Journal of Arid Environments*, *73*(11), 963–977. https://doi.org/10.1016/j.jaridenv.2009.04.022

Liu, Z., Huang, J., Xiao, X., & Tong, X. (2022). The capability of CMIP6 models on seasonal precipitation extremes over Central Asia. *Atmospheric Research*, *278*, 106364. https://doi.org/10.1016/j.atmosres.2022.106364

Luo, M., Liu, T., Meng, F., Duan, Y., Bao, A., Frankl, A., & De Maeyer, P. (2019). Spatiotemporal characteristics of future changes in precipitation and temperature in Central Asia. *International Journal of Climatology*, *39*(3), 1571–1588. https://doi.org/10.1002/joc.5901

Lyu, K., Zhang, X., Church, J. A., Slangen, A. B. A., & Hu, J. (2014). Time of emergence for regional sea-level change. *Nature Climate Change*, *4*(11), 1006–1010. https://doi.org/10.1038/nclimate2397

Man, W., Zhou, T., & Jungclaus, J. H. (2014). Effects of large volcanic eruptions on global summer climate and East Asian monsoon changes during the last millennium: Analysis of MPI-ESM simulations. *Journal of Climate*, *27*(19), 7394–7409. https://doi.org/10.1175/JCLI-D-13-00739.1

Menne, M. J., Durre, I., Vose, R. S., Gleason, B. E., & Houston, T. G. (2012). An overview of the global historical climatology network-daily database [Dataset]. *Journal of Atmospheric and Oceanic Technology*, *29*(7), 897–910. https://doi.org/10.1175/JTECH-D-11-00103.1

Oki, T., & Kanae, S. (2006). Global hydrological cycles and world water resources. *Science*, *313*(5790), 1068–1072. https://doi.org/10.1126/science.1128845

Peng, D., Zhou, T., Zhang, L., & Wu, B. (2018). Human contribution to the increasing summer precipitation in Central Asia from 1961 to 2013. *Journal of Climate*, *31*(19), 8005–8021. https://doi.org/10.1175/JCLI-D-17-0843.1

Peng, D., Zhou, T., Zhang, L., Zhang, W., & Chen, X. (2019). Observationally constrained projection of the reduced intensification of extreme climate events in Central Asia from 0.5°C less global warming. *Climate Dynamics*, *54*(1–2), 543–560. https://doi.org/10.1007/s00382-019-05014-6

Qin, M., Dai, A., & Hua, W. (2020). Quantifying contributions of internal variability and external forcing to Atlantic Multidecadal Variability since 1870. *Geophysical Research Letters*, *47*(22), e2020GL089504. https://doi.org/10.1029/2020GL089504

Rayner, N., Parker, D. E., Horton, E., Folland, C. K., Alexander, L. V., Rowell, D., et al. (2003). Global analyses of sea surface temperature, sea ice, and night marine air temperature since the late nineteenth century [Dataset]. *Journal of Geophysical Research*, *108*(D14), 4407. https://doi.org/10.1029/2002JD002670

Risser, M. D., Collins, W. D., Wehner, M. F., O'Brien, T. A., Huang, H., & Ullrich, P. A. (2024). Anthropogenic aerosols mask increases in US rainfall by greenhouse gases. *Nature Communications*, *15*(1), 1318. https://doi.org/10.1038/s41467-024-45504-8

Schneider, U., Hänsel, S., Finger, P., Rustemeier, E., & Ziese, M. (2022). GPCC full data monthly product version 2022 at 0.5°: Monthly land-surface precipitation from rain-gauges built on GTS-based and historical data [Dataset]. *Global Precipitation Climatology Centre (GPCC)*. https://doi.org/10.5676/DWD_GPCC/FD_M_V2022_050

Song, F., Zhou, T., & Qian, Y. (2014). Responses of East Asian summer monsoon to natural and anthropogenic forcings in the 17 latest CMIP5 models. *Geophysical Research Letters*, *41*(2), 596–603. https://doi.org/10.1002/2013GL058705

Song, S., & Bai, J. (2016). Increasing winter precipitation over arid Central Asia under global warming. *Atmosphere*, *7*(10), 139. https://doi.org/10.3390/atmos7100139

Steinman, B. A., Mann, M. E., & Miller, S. K. (2015). Atlantic and Pacific multidecadal oscillations and Northern Hemisphere temperatures. *Science*, *347*(6225), 988–991. https://doi.org/10.1126/science.1257856

Swinnen, J., Burkitbayeva, S., Schierhorn, F., Prishchepov, A. V., & Müller, D. (2017). Production potential in the "bread baskets" of Eastern Europe and Central Asia. *Global Food Security*, *14*, 38–53. https://doi.org/10.1016/j.gfs.2017.03.005

Takaya, K., & Nakamura, H. (2001). A formulation of a phase-independent wave-activity flux for stationary and migratory quasigeostrophic eddies on a zonally varying basic flow. *Journal of the Atmospheric Sciences*, *58*(6), 608–627. https://doi.org/10.1175/1520-0469(2001)058<0608:AFOAPI>2.0.CO;2

Tebaldi, C., & Knutti, R. (2007). The use of the multi-model ensemble in probabilistic climate projections. *Philosophical Transactions of the Royal Society A*, *365*(1857), 2053–2075. https://doi.org/10.1098/rsta.2007.2076

Undorf, S., Bollasina, M. A., & Hegerl, G. C. (2018). Impacts of the 1900–74 increase in anthropogenic aerosol emissions from North America and Europe on Eurasian summer climate. *Journal of Climate*, *31*(20), 8381–8399. https://doi.org/10.1175/JCLI-D-17-0850.1

Wang, T., Xu, H., Jiang, D., & Yao, J. (2022). Mechanisms of reduced mid-holocene precipitation in arid central Asia as simulated by PMIP3/4 models. *Journal of Geophysical Research: Atmospheres*, *127*(8), e2021JD036153. https://doi.org/10.1029/2021JD036153

Wei, Y., & Yu, H. (2024). The interdecadal weakening of the relationship between Indian Ocean Sea surface temperature and summer precipitation in Central Asia. *Geophysical Research Letters*, *51*(4), e2023GL107371. https://doi.org/10.1029/2023gl107371

Williams, E. L., Abatzoglou, J. T., Hegewisch, K. C., & Williams, A. P. (2024). Anthropogenic climate change has reduced drought recovery probabilities across the western US. *Communications Earth & Environment*, *5*(1), 546. https://doi.org/10.1038/s43247-024-01640-z

Xie, X., Myhre, G., Shindell, D., Faluvegi, G., Takemura, T., Voulgarakis, A., et al. (2022). Anthropogenic sulfate aerosol pollution in South and East Asia induces increased summer precipitation over arid Central Asia. *Communications Earth & Environment*, *3*(1), 328. https://doi.org/10.1038/s43247-022-00660-x

Yan, X., Zhang, Q., Ren, X., Wang, X., Yan, X., Li, X., et al. (2022). Climatic change characteristics towards the "Warming–Wetting" trend in the pan-central-asia arid region. *Atmosphere*, *13*(3), 467. https://doi.org/10.3390/atmos13030467

Yang, Y., & He, L. (2019). Agricultural product consumption and trade dataset of the Five Central Asia Countries (1992–2016) [Dataset]. https://doi.org/10.11888/HumanNat.tpdc.272764

Yao, J., & Chen, Y. (2015). Trend analysis of temperature and precipitation in the Syr Darya Basin in Central Asia. *Theoretical and Applied Climatology*, *120*(3), 521–531. https://doi.org/10.1007/s00704-014-1187-y

Yao, M., Tang, H., Huang, G., & Wu, R. (2024). Interdecadal shifts of ENSO influences on spring Central Asian precipitation. *npj Climate and Atmospheric Science*, *7*(1), 194. https://doi.org/10.1038/s41612-024-00742-x

Yu, X., Luo, H., Wang, H., & Feil, J.-H. (2020). Climate change and agricultural trade in central Asia: Evidence from Kazakhstan. *Ecosystem Health and Sustainability*, *6*(1), 1766380. https://doi.org/10.1080/20964129.2020.1766380

Zhang, S., Liu, X., & Dong, B. (2024). Spatiotemporal characteristics of the time of emergence for anthropogenic tropospheric temperature changes based on the CMIP6 multi-model results. *Environmental Research Letters*, *19*(4), 044052. https://doi.org/10.1088/1748-9326/ad34e6

Zhu, X., Wei, Z., Dong, W., Ji, Z., Wen, X., Zheng, Z., et al. (2020). Dynamical downscaling simulation and projection for mean and extreme temperature and precipitation over central Asia. *Climate Dynamics*, *54*(7–8), 3279–3306. https://doi.org/10.1007/s00382-020-05170-0